

Interpreting the seasonality of atmospheric methane

James D. East¹, Daniel J. Jacob¹, Nicholas Balasus¹, A. Anthony Bloom², Lori P. Bruhwiler³, Zichong Chen¹, Jed O. Kaplan⁴, Loretta J. Mickley¹, Todd A. Mooring⁵, Elise Penn⁵, Benjamin Poulter⁶, Melissa Payer Sulprizio¹, Robert M. Yantosca¹, John R. Worden², and Zhen Zhang⁷

¹Harvard John A. Paulson School of Engineering and Applied Sciences

²Jet Propulsion Laboratory, California Institute of Technology

³National Oceanic and Atmospheric Administration (NOAA)

⁴Department of Earth, Energy, and Environment, University of Calgary

⁵Department of Earth and Planetary Sciences, Harvard University

⁶NASA GSFC, Biospheric Sciences Lab

⁷State Key Laboratory of Tibetan Plateau Earth System, Environment and Resources (TPESER), Institute of Tibetan Plateau Research, Chinese Academy of Sciences

April 16, 2024

Abstract

Surface and satellite observations of atmospheric methane show smooth seasonal behavior in the Southern Hemisphere driven by loss from the hydroxyl (OH) radical. However, observations in the Northern Hemisphere show a sharp mid-summer increase that is asymmetric with the Southern Hemisphere and not captured by the default configuration of the GEOS-Chem chemical transport model. Using an ensemble of 22 OH model estimates and 24 wetland emission inventories in GEOS-Chem, we show that the magnitude, latitudinal distribution, and seasonality of Northern Hemisphere wetland emissions are critical for reproducing the observed seasonality of methane in that hemisphere, with the interhemispheric OH ratio playing a lesser role. Reproducing the observed seasonality requires a wetland emission inventory with ~ 80 Tg a⁻¹ poleward of 10°N including significant emissions in South Asia, and an August peak in boreal emissions persisting into autumn. In our 24-member wetland emission ensemble, only the LPJ-wsl MERRA-2 inventory has these attributes.

Interpreting the seasonality of atmospheric methane

James D. East¹, Daniel. J. Jacob¹, Nicholas Balasus¹, A. Anthony Bloom², Lori Bruhwiler³, Zichong Chen¹, Jed O. Kaplan⁴, Loretta J. Mickley¹, Todd A. Mooring⁵, Elise Penn⁵, Benjamin Poulter⁶, Melissa P. Sulprizio¹, Robert M. Yantosca¹, John R. Worden², Zhen Zhang⁷

¹ Harvard John A. Paulson School of Engineering and Applied Sciences, Harvard University, Cambridge, MA, USA, 02138

² Jet Propulsion Laboratory, California Institute of Technology, Pasadena, CA, USA 91011

³ NOAA Earth System Research Laboratory, Global Monitoring Division, Boulder, CO, USA 80305

⁴ Department of Earth, Energy, and Environment, University of Calgary, Calgary, Canada

⁵ Department of Earth and Planetary Sciences, Harvard University, Cambridge, MA, USA 02138

⁶ NASA GSFC, Biospheric Sciences Lab, Greenbelt, MD 20771

⁷ State Key Laboratory of Tibetan Plateau Earth System, Environment and Resources (TPESER), Institute of Tibetan Plateau Research, Chinese Academy of Sciences, Beijing, China

Corresponding author: J. D. East, jeast@g.harvard.edu

Key Points:

- Northern Hemisphere atmospheric methane shows a summer increase not replicated by the GEOS-Chem model with its default sources and sinks
- The summer increase's timing and magnitude is determined by the magnitude, seasonality, and spatial distribution of NH wetland emissions
- Inversions of atmospheric methane observations should use a suitable wetland emission inventory and optimize hemispheric OH concentrations

Abstract

Surface and satellite observations of atmospheric methane show smooth seasonal behavior in the Southern Hemisphere driven by loss from the hydroxyl (OH) radical. However, observations in the Northern Hemisphere show a sharp mid-summer increase that is asymmetric with the Southern Hemisphere and not captured by the default configuration of the GEOS-Chem chemical transport model. Using an ensemble of 22 OH model estimates and 24 wetland emission inventories in GEOS-Chem, we show that the magnitude, latitudinal distribution, and seasonality of Northern Hemisphere wetland emissions are critical for reproducing the observed seasonality of methane in that hemisphere, with the interhemispheric OH ratio playing a lesser role. Reproducing the observed seasonality requires a wetland emission inventory with $\sim 80 \text{ Tg a}^{-1}$ poleward of 10°N including significant emissions in South Asia, and an August peak in boreal emissions persisting into autumn. In our 24-member wetland emission ensemble, only the LPJ-wsl MERRA-2 inventory has these attributes.

Plain Language Summary

The amount of methane, a powerful greenhouse gas, has been growing in Earth's atmosphere during the last decade, and scientists disagree about which methane sources and sinks are responsible for the growth. One clue into understanding methane's sources and sinks is their seasonality – their month-to-month cycles that happen every year. Measurements of atmospheric methane taken at the Earth's surface and using satellite instruments show a steep increase each summer in the Northern Hemisphere that is not replicated when methane is simulated in a global chemical transport model, indicating missing information about source and sink seasonalities. To investigate, we use that model to simulate 24 representations of methane's largest source, emissions from wetlands, and 22 representations of its largest sink, chemical loss by the hydroxyl radical (OH). We find that OH is unlikely to cause the summer increase and model bias, but the amount, spatial distribution, and seasonal cycles of global wetland emissions are the strongest drivers. We suggest that these characteristics are linked to the underlying mechanisms determining wetland area and methane production in wetland models. The results unveil the role of global wetlands in driving methane's seasonality and inform research to analyze methane's long-term trends.

1 Introduction

Methane (CH_4) is a greenhouse gas with a global warming potential 80 times that of CO_2 on a 20-year time scale, and an atmospheric abundance that has been increasing at an accelerated pace in recent years (IPCC, 2021). Uncertainty in the methane budget makes it difficult to identify drivers of methane's recent growth (Kirschke et al., 2013; Saunio et al., 2020; Turner et al., 2017). Inverse analyses using atmospheric methane observations have been used extensively to quantify methane sources and sinks (Houweling et al., 2017; Jacob et al., 2016; Palmer et al., 2021), but require prior assumptions regarding the behavior and seasonality of these sources and sinks. Here, we show that the observed seasonality of atmospheric methane places basic constraints on the methane budget that should be reflected in the prior estimates used for inversions.

The observed seasonality of atmospheric methane offers important information on the methane budget (Chandra et al., 2017; Dowd et al., 2023; Kivimäki et al., 2019; Warwick et al., 2016) because several budget terms have strong seasonal variations, including emissions from wetlands (Delwiche et al., 2021; Ito et al., 2023; Parker et al., 2020; Rocher-Ros et al., 2023), rice cultivation (Zhang et al., 2016a; Zhang et al., 2020), manure (Chadwick et al., 2011), and fires (Van Der Werf et al., 2017), as well as losses to oxidation by the hydroxyl radical (OH) (Dlugokencky et al., 1997; Naus et al., 2021) and soil

uptake (Murguia-Flores et al., 2018; Nazaries et al., 2013). Global chemical transport models used as forward models in inverse analyses have difficulty reproducing the observed seasonality of atmospheric methane (Maasakkers et al., 2019; Pickett-Heaps et al., 2011; Warwick et al., 2016).

Inverse analyses either seek to correct the seasonalities of the methane budget terms or treat them as parameters, meaning that they are not optimized and are instead considered to be part of the forward model error. Treating seasonalities as model parameters provides more power for the inversion to constrain other aspects of the methane budget, but bias in the prior estimate can persist to the inversion results (Yu et al., 2021). Even when seasonalities are optimized in the inversion, the associated error covariances between budget terms can complicate the optimization (Bergamaschi et al., 2018; Tsuruta et al., 2023; Zhang et al., 2021), and

Here, we use global surface and satellite observations of the seasonality of atmospheric methane, simulated with the GEOS-Chem chemical transport model, to better understand the roles of different methane budget terms in driving the seasonality and the implications for inverse analyses. Surface observations are from the remote sites of the NOAA network (Schuldt et al., 2023) and satellite observations are from a blended TROPOMI+GOSAT dry air column mole fraction (XCH_4) retrieval that combines the observational density of the TROPOMI instrument with the precision of the GOSAT instrument (Balasus et al., 2023). GEOS-Chem is widely used as forward model in global and regional inverse analyses (e.g., Chen et al., 2023; Feng et al., 2023; Worden et al., 2022; Zhang et al., 2022). We show that GEOS-Chem driven by its default prior budget terms has a large seasonal bias in the northern hemisphere. We then explore the contribution of individual budget terms to this bias using simulation ensembles. This leads us to recommend improved choices of prior budget terms for use in inverse analyses.

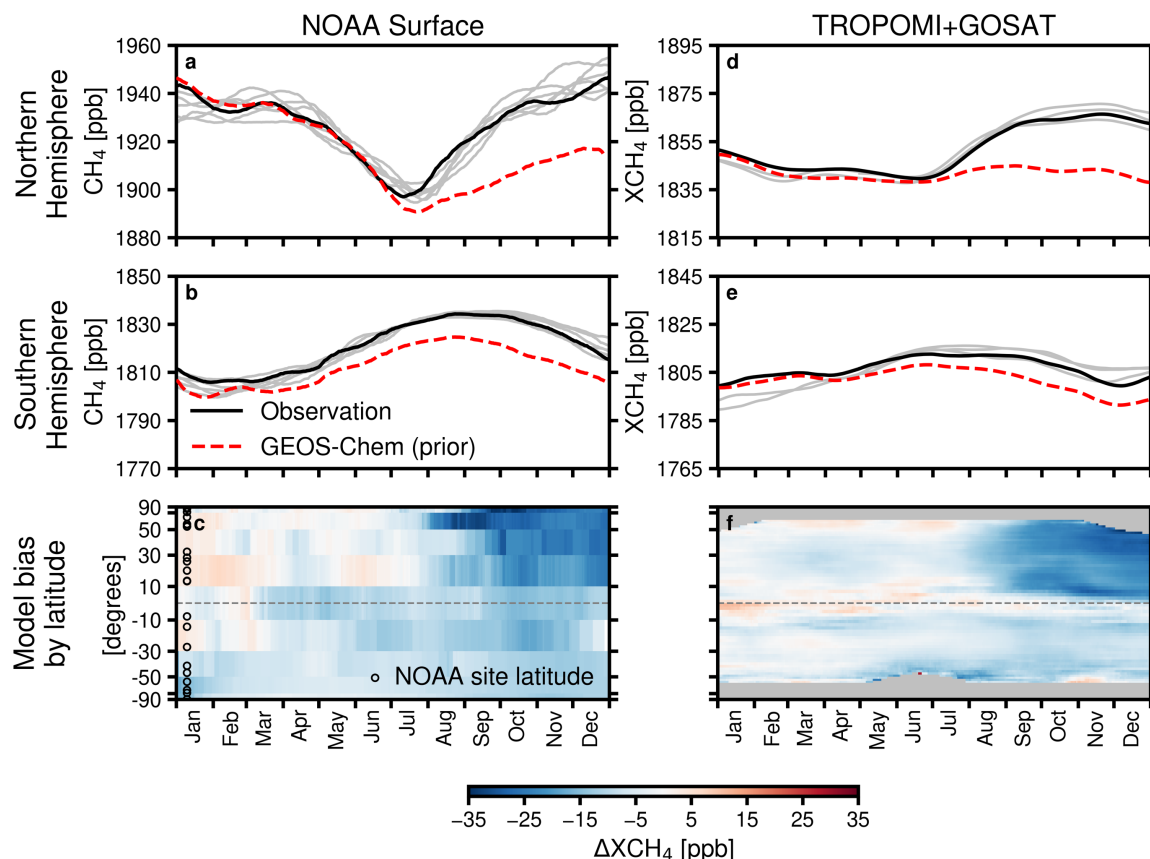


Figure 1: Seasonality of atmospheric methane concentrations in the Northern and Southern Hemispheres. The 2019 observations from the NOAA remote surface sites (<https://gml.noaa.gov/ccgg/mb/mb.html>) and from blended TROPOMI+GOSAT satellite retrievals of the dry air column mole fraction XCH_4 (Balasus et al., 2023) are compared to the GEOS-Chem model driven by its default budget terms (Table 1) and sampled in the same way as the observations. Panels (a) and (b) show the daily hemispheric averages from the NOAA Marine Boundary Layer (MBL) Reference, constructed from the mean of each day's observations across all sites in the hemisphere. Panels (d) and (e) show valid TROPOMI+GOSAT observations over land, discarding observations above $60^\circ N$ and below $60^\circ S$, which are affected by high uncertainty. To create the curves, satellite retrievals are first binned and then averaged into GEOS-Chem $2^\circ \times 2.5^\circ$ grid cells each day. Daily, area-weighted zonal means are then created from the binned data. Curves in (a, b, d, e) show results from two passes of a 30-day moving average filter, with black curves denoting observations and red dashed curves representing model results. Grey lines denote interannual variability for 2015 – 2021 NOAA measurements and for May 2018 – December 2021 TROPOMI+GOSAT retrievals (the TROPOMI record starts in May 2018), with the annual averages adjusted to match the 2019 mean. Panel (c) shows the model bias (model minus observations) in surface concentrations compared to NOAA MBL observations in 20° latitude bands, and panel (f) shows the same compared to TROPOMI+GOSAT XCH_4 . Data in (c) and (f) is plotted as sine latitude. Note different y-axes in panels a, b, d, e.

2 Seasonality of atmospheric methane

Figure 1 (a and b) shows the observed seasonal variations of surface methane in the Northern Hemisphere (NH) and Southern Hemisphere (SH). Observations are methane surface flask samples

between 2015 and 2021 from the NOAA Marine Boundary Layer (MBL) Reference (NOAA GML, 2023) accessed via CH₄ GLOBALVIEWplus v5.1 ObsPack (Schuldt et al., 2023). The seasonality is highly consistent from year to year. The SH February-March minimum and August-September maximum can simply be explained by the OH sink, and are similar to those of methyl chloroform, which is commonly used as a global OH proxy (Patra et al., 2021). The NH seasonality is more complex, featuring a sharp July minimum rather than a smooth seasonal cycle in opposite phase to the SH.

Table 1: Global methane budget¹

Budget term	GEOS-Chem default (2019)	Global Carbon Project (2017)
Sources (Tg a⁻¹)	528	747 [602-896]
Wetlands*	147 ²	145 [100-183]
Other natural sources ³	14	222 [143-306]
Agriculture & waste	240 ⁴	213 [198-232]
Enteric fermentation & manure	121	115 [110-121]
Enteric fermentation	109	
Manure management*	12	
Landfills, wastewater	81 ⁴	68 [64-71]
Rice cultivation*	38 ⁴	30 [24-40]
Fossil fuels	84 ⁵	135 [121-164]
Other anthropogenic	24 ⁴	
Fires*	19 ⁶	29 [24-38]
Sinks (Tg a⁻¹)	545	625 [500-798]
Chemical loss (sink)*	511 ⁷	595 [498-749]
Tropospheric OH *	471	
Stratospheric loss*	37	
Tropospheric Cl*	3	
Soil uptake (sink)*	34 ⁸	30 [11-49]
Lifetime against tropospheric OH (years)	11.2	

* Assumed to be seasonally varying in GEOS-Chem.

¹ GEOS-Chem default sources and sinks used as prior estimates in inversions, and bottom-up central estimates and ranges from the Global Carbon Project (GCP) (Saunio et al., 2020)

² WetCHARTs version 1.3.3 ensemble (Bloom et al., 2017), using the mean of the nine best performing ensemble members (Ma et al., 2021)

³ Termites and other wild animals, water bodies, and geological seeps. The large GCP bottom-up estimate is due mostly to lakes and is not supported by top-down estimates (Saunio et al., 2020)

⁴ EDGAR v6 (Crippa et al., 2020) superseded by national estimates for the US, Canada, and Mexico (Maasakkers et al., 2016; Scarpelli et al., 2020; Scarpelli et al., 2022a)

⁵ GFEI v2 (Scarpelli et al., 2022b) based on national totals reported to the United Nations Framework Convention on Climate Change (UNFCCC).

⁶ GFED version 4 (Van Der Werf et al., 2017)

⁷ Chemical losses computed from GEOS-Chem oxidant fields including tropospheric OH from Wecht et al. (2014), stratospheric oxidants from Eastham et al. (2014), tropospheric Cl from Wang et al. (2019). GEOS-Chem has an atmospheric methane lifetime of 11.2 years from oxidation by tropospheric OH, consistent with the lifetime of 11.2 ± 1.3 years inferred from methyl chloroform observations (Prather et al., 2012).

⁸ MeMo v1.0 global model (Murguia-Flores et al., 2018)

Figure 1 also compares the NOAA observations to the methane seasonality simulated by GEOS-Chem for 2019 with its default sources and sinks used as prior estimates in recent inverse analyses. GEOS-Chem is sampled at the NOAA sites and the hemispheric means are computed with the same procedure used with the observational data. Table 1 shows the methane sources and sinks used in the default simulation, and compares with the multi-model bottom-up estimates for 2017 compiled by the Global Carbon Project (Saunio et al., 2020). The GCP has a larger global source mainly because it assumes large emissions from lakes, but these are not supported by top-down inversion estimates (Saunio et al., 2020). We use GEOS-Chem version 14.1.0 (doi.org/10.5281/zenodo.7600404) at

2° × 2.5° horizontal resolution with NASA MERRA-2 assimilated meteorological data. Initial conditions on December 1, 2018, are from a 34-year GEOS-Chem simulation that uses time-varying gridded NOAA surface methane observations as its lower boundary condition. We do this to properly initialize the stratosphere, in which transport time scales are several years (Mooring et al., 2024). To account for regional emissions-driven methane enhancements not adequately resolved by the surface boundary condition, we conduct a 1-month spinup for December 2018 and then apply a bias correction to the 3-D methane mole fractions at the spinup's last timestep using zonally averaged TROPOMI+GOSAT observations over land grid cells. The resulting initialization is unbiased with respect to surface and satellite methane observations in the NH and SH.

The GEOS-Chem seasonality in the SH is consistent with the NOAA observations (Figure 1b). There is a gradual departure from the observations that can be attributed to a global bias in the default bottom-up sources and/or sinks used in GEOS-Chem. Such a bias is expected (Saunio et al., 2020) and would be corrected in an inversion (Zhang et al., 2021). The lack of seasonal dependence of the bias indicates that the driver of SH seasonality – mainly loss to OH – is well represented in the model. On the other hand, the GEOS-Chem seasonality in the NH does not capture the sharp rise starting in July and the resulting offset persists for the rest of the year (Figure 1a).

Figure 1 (d and e) shows the seasonality of XCH₄ in each hemisphere for the blended TROPOMI+GOSAT satellite observations (Balasus et al., 2023) and for GEOS-Chem sampled at the same locations. The seasonality is similar to that in the NOAA data. The satellite data have a smaller relative seasonal amplitude because of their lower range of latitudes and because of the dominance of the lower troposphere for the methane sink resulting from the strong temperature dependence of the CH₄ + OH rate constant. The model matches the observed seasonality until July but fails to reproduce the sharp rise starting that month.

Figure 1 (c and f) further shows the seasonal and latitudinal dependence of the model bias relative to the NOAA and TROPOMI+GOSAT observations. The SH shows a weak negative bias slowly growing with time versus both surface and satellite. The NH bias versus the NOAA data starts with a sharp onset at 50°N-70°N in August that then spreads within a month to the rest of the hemisphere. No such latitudinal structure in the bias is found for the TROPOMI+GOSAT data (restricted to south of 60°), where onset of the bias is in August across the NH.

169 3 Drivers of methane seasonality

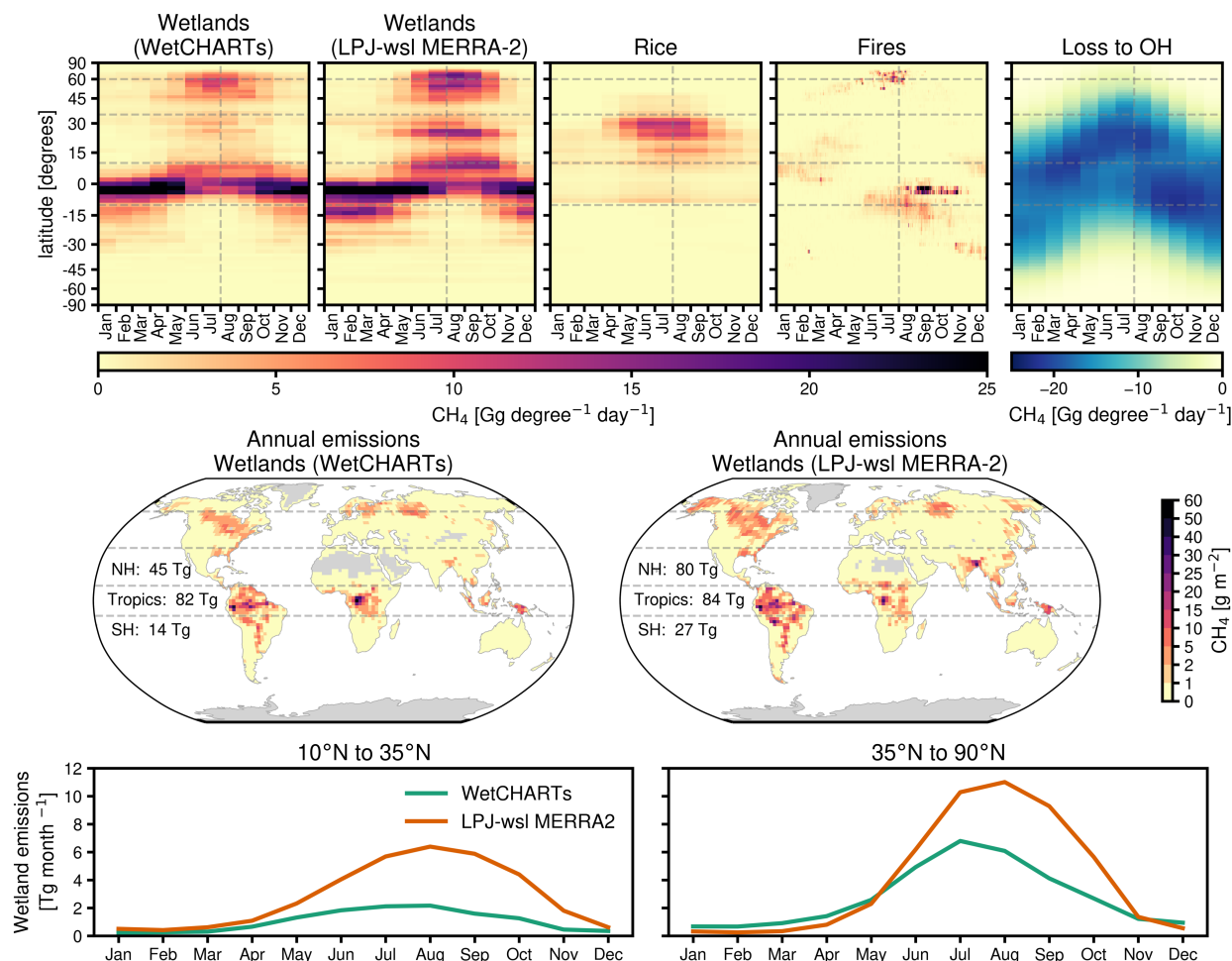


Figure 2: Seasonal cycles of major seasonally varying terms in the GEOS-Chem methane budget for 2019. Top row shows monthly zonal sums plotted versus latitude. Horizontal dashed lines at 10°S, 10°N, 35°N, and 60°N delimit the latitude bands used in the analysis, and the vertical dashed line is at August 1st. The WetCHARTs wetland emissions are the mean of the nine best-performing ensemble members (Ma et al., 2021). Maps show the distribution of annual emissions from WetCHARTs (mean of the nine members of the high-performing ensemble) and LPJ-wsl MERRA-2, with annual total emissions for latitude bands 90°S-10°S, 10°S-10°N, and 10°N-90°N inset. The bottom row shows the corresponding monthly wetland emissions in the 10°-35°N and 35°-60°N latitude bands.

Here we aim to understand the drivers of the methane seasonality in the NH and the cause of the sharp mid-summer rise. Figure 2 shows the seasonal and latitudinal distributions of seasonally varying budget terms in GEOS-Chem including emissions from wetlands, rice cultivation, and fires, and loss to tropospheric OH. We focus on OH and wetlands as the dominant seasonally varying terms and use ensembles of independent estimates of these terms as estimates of uncertainty. We compare the resulting simulations to the TROPOMI+GOSAT observations, which are of particular value for inversions, focusing on the 10°-35°N and 35°-60°N latitude bands where discrepancies between model and observations are most prominent.

Loss by OH

Figure 3 compares TROPOMI+GOSAT XCH₄ observations to XCH₄ calculated by an ensemble of GEOS-Chem simulations using global 3-D monthly mean OH concentrations archived from 17 different atmospheric chemistry models that contributed to the Atmospheric Chemistry and Climate Model Intercomparison Project (ACCMIP) (12 models; Naik et al., 2013) and the Chemistry-Climate Model Initiative (CCMI) Phase-1 (5 models; Hegglin et al., 2015; Orbe et al., 2020). Individual models are listed in Table S1 and are described in Lamarque et al. (2013) for ACCMIP and Morgenstern et al. (2017) for CCMI. All OH fields are scaled so that methane's tropospheric lifetime due to loss to OH matches the best estimate derived from methyl chloroform observations of 11.2 years (Prather et al., 2012). We do this for each archived OH field by performing a 1-year GEOS-Chem simulation without scaling OH, calculating the methane lifetime, and then applying a single global scaling factor to adjust OH concentrations to yield the expected methane lifetime of 11.2 years. This ensures that differences between the OH fields in our ensemble are due to their seasonality and distribution, and not due to differences in methane lifetime. In addition, we perform two simulations with the GEOS-Chem default OH field perturbed $\pm 10\%$, representing an estimate of the uncertainty for global mean OH (Prather et al., 2012).

Figure 3 shows that all OH models yield the same methane seasonality in the NH. All models capture the observed methane seasonality in the first half of the year and none capture the mid-summer rise, which would require a sharp decrease in OH not simulated by any of the models. However, there is evidence that lower model NH/SH OH interhemispheric ratios can lead to a better comparison against observations. The model NH/SH OH ratios range from 1.07 to 1.40 (Table S1 and Figure S1; 1.07 for the GEOS-Chem default), while methyl chloroform observations imply a ratio of 0.97 ± 0.12 (Patra et al., 2014). We investigate this possibility by applying hemispheric scale factors to the GEOS-Chem OH fields to achieve annual mean NH/SH ratios of 0.97 and 0.85 in two separate simulations. This is accomplished by adjusting NH OH concentrations to get the desired annual mean NH/SH ratio, and then performing a GEOS-Chem simulation to calculate a global scaling factor which is applied to yield a tropospheric methane lifetime to OH of 11.2 years, as before. Figure 3 shows that lower OH concentrations in the NH allow for an increase of NH methane in mid-summer, leading to a better match at $10^\circ - 35^\circ\text{N}$. However, at $35^\circ - 60^\circ\text{N}$ the increase starts earlier than the observations, and the underestimate of observations later in the summer is merely delayed. In addition, bias in the SH gets worse with higher OH in that hemisphere (Figure S2). Figure 3 also shows that decreasing global OH by 10% produces a better match to end-of-year observations in our simulations, but the seasonal cycle amplitude is severely under estimated. Adjusting OH within its $\pm 10\%$ uncertainty does not improve simulations of methane's seasonality.

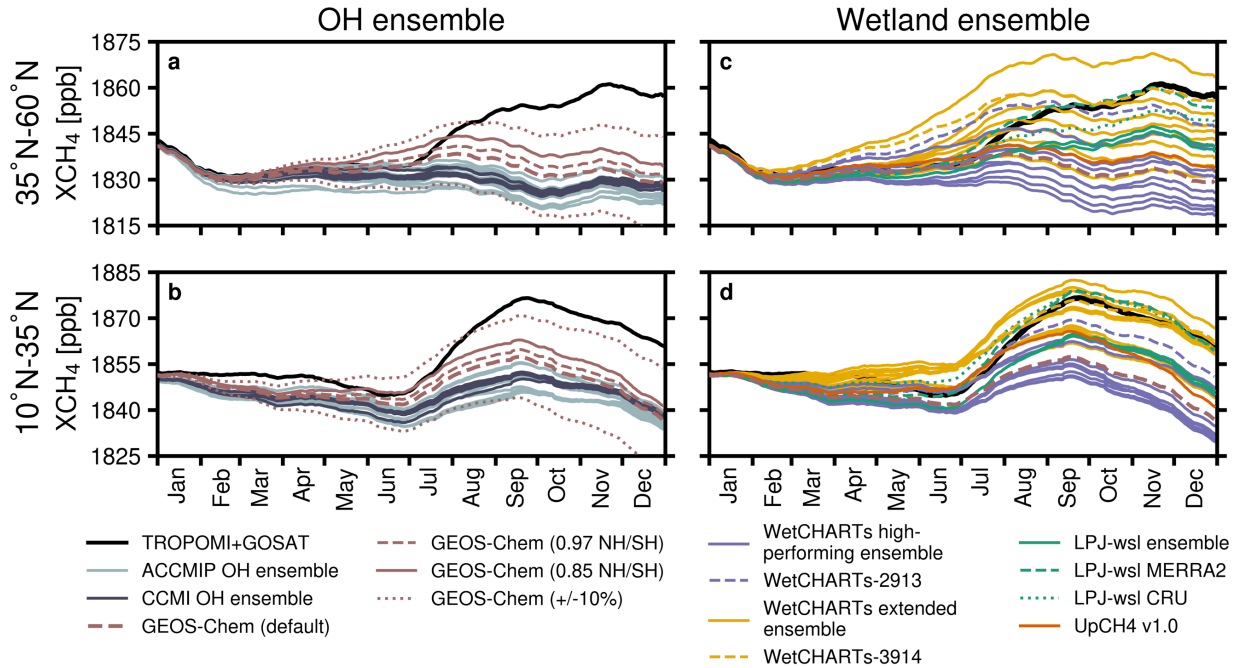


Figure 3: Seasonality of dry air column mole fraction of methane (XCH_4) for ensembles of OH and wetland simulations, compared to TROPOMI+GOSAT observations (black curves) for the $10^\circ N$ - $35^\circ N$ and $35^\circ N$ - $60^\circ N$ latitude bands. Panels (a) and (b) show results for the OH ensemble with colored curves representing results from different model simulations, and panels (c) and (d) show results for the wetland emissions ensemble. All OH concentrations except for the dotted lines ($\pm 10\%$) have been normalized to yield a methane lifetime of 11.2 years against oxidation by tropospheric OH. Brown curves in panels (a) and (b) show GEOS-Chem with its default OH which has a NH/SH ratio of 1.07, simulations with global mean OH adjusted $\pm 10\%$, and additional simulations with the NH/SH ratio adjusted to 0.97 and 0.85. Dashed and dotted curves in panels (c) and (d) show XCH_4 simulated with selected wetland ensemble members including WetCHARTs-2913, WetCHARTs-3914, LPJ-wsl MERRA-2, and LPJ-wsl CRU.

Emissions from wetlands

We conducted an ensemble of 24 simulations with different monthly wetland emission inventories. In addition to the base run, the ensemble includes (1) four inventories from the Lund–Potsdam–Jena Wald Schnee und Landschaft (LPJ-wsl) dynamic global vegetation model (Zhang et al., 2016b) driven with assimilated meteorological data from either MERRA-2, CRU, ERA5, or ERA5 with MSWEP precipitation; (2) 18 inventories from the full WetCHARTs v1.3.3 ensemble (Bloom et al., 2017), including the nine highest-performing (HP) WetCHARTs members identified in Ma et al. (2021); and (3) the UpCH4 v1.0 inventory applying machine learning to generalize flux tower observations (McNicol et al., 2023). The inventory in our base run is the mean of the HP WetCHARTs members. Table S2 gives the annual wetland emissions for each member and the peak month for boreal emissions north of $35^\circ N$.

Figure S2 shows methane in the Southern Hemisphere and the tropics for the wetland emissions ensemble. The simulations all exhibit similar seasonality to the GEOS-Chem default. In the tropics ($10^\circ S$ – $10^\circ N$), LPJ-wsl MERRA-2 performs best among all flux estimates, while LPJ-wsl CRU and several members of the WetCHARTs extended ensemble are notably high-biased throughout the year.

Figure 3 (c and d) shows NH methane simulated with the wetland ensemble. The spread of seasonality is much larger than for the ensemble of OH models, reflecting differences in the latitude-

dependent timing and magnitude of wetland emissions. We find that the LPJ-wsl MERRA-2 is uniquely successful in reproducing the observed seasonality in the two latitude bands. LPJ-wsl CRU simulates 10°N – 35°N seasonality well but underestimates observations north of 35°. UpCH4 is biased low throughout the NH and does not replicate observed seasonality at 35°-60°N. WetCHARTs members 2913 and 3914, symbolized with dashed lines in Figure 3, perform best among the WetCHARTs ensemble members. However, both exhibit a large spring high bias at 35°-60°N, and WetCHARTs-2913 results in a subsequent underestimate compared to observations.

Several features in the magnitude and timing of emissions from LPJ-wsl MERRA-2 distinguish it from the other estimates. First, it has larger NH emissions than any of the other inventories, with 80 Tg north of 10°N and over half of those emissions occurring north of 35°N. Second, larger regional emissions from South Asia compared to the other inventories, particularly in July – October, contribute to better seasonality at 10°-35°N. Third, LPJ-wsl's boreal emissions have a delayed emissions onset, an August peak (versus a July peak in WetCHARTs and UpCH4), and larger emissions through the boreal autumn.

The inventories differ in their meteorological inputs and the degree to which they represent physical processes controlling emissions. LPJ-wsl's delayed summer peak and sustained autumn boreal emissions, in line with observed high-latitude wetland dynamics (Bao et al., 2021; Warwick et al., 2016) and global wetland methane flux observations (Chang et al., 2021), are due to its permafrost module (Zhang et al., 2016b) which allows the use of soil temperature for estimating heterotrophic respiration. In contrast, WetCHARTs' methanogenesis and heterotrophic respiration parameterizations (Bloom et al., 2016) rely on air temperature. Soil temperature seasonal changes lag air temperature changes, allowing LPJ-wsl to better represent freeze-thaw and permafrost dynamics (Wania et al., 2009), which in turn control the timing and magnitude of boreal wetland emissions through changes in soil moisture and temperature (Olefeldt et al., 2013; Treat et al., 2018). In addition, LPJ-wsl explicitly simulates snow-cover, which may suppress spring boreal wetland emissions (Pickett-Heaps et al., 2011). Although emissions from rice and wetlands are difficult to distinguish in South Asia (Peters et al., 2017), LPJ-wsl MERRA-2's higher emissions may stem from better representation of wetland area through its inundation model and rice cultivation masking (Portmann et al., 2010). WetCHARTs, using GLWD as its wetland map, may underestimate wetland extent in the region. Among LPJ-wsl members, NH emissions driven by MERRA-2 meteorology are larger than those driven by CRU, ERA5, or ERA5-MSWEP because of differences in precipitation and temperature (Zhang et al., 2018).

Other potential drivers of methane seasonality

Rice emissions are concentrated in the 10°-35°N latitude band of South Asia, and EDGAR v6 emissions used in GEOS-Chem by default peak in July (Figure 2). Inversions of GOSAT and TROPOMI satellite data indicate that peak emissions should be shifted to later in the season (Palmer et al., 2021; Yu et al., 2023). We tested shifting EDGARv6 rice emissions seasonality to July-October and increasing their magnitude, as shown in Figure S3, but the effects are limited by the relatively small magnitude of rice emissions. Increasing this magnitude further would not be consistent with the range of Global Carbon Project estimates (Table 1). In addition, Figure 1 shows no indication that the NH bias is initiated at rice-growing latitudes.

Boreal wildfires are a NH source of atmospheric methane with a seasonal peak in late summer to fall (Liu et al., 2020; Nelson et al., 2021; Turetsky et al., 2004), but the source is relatively small (Figure 2). Carbon monoxide (CO) observations at the NOAA sites show interannual variability associated with high fire years but we cannot detect correlated interannual variability for methane in the NOAA data.

The soil sink for methane has a seasonality largely controlled by temperature, and the northern mid-latitudes exhibit the largest seasonal variations with peak uptake in summer (Curry, 2007; Murguía-Flores et al., 2018; Priemé & Christensen, 1997). Soil uptake in the NH north of 10°N is estimated at 19 Tg per year (Murguía-Flores et al., 2018), which is too small to significantly affect the methane seasonality. Emissions from landfills may vary seasonally and these variations need to be better understood, but the amplitude would likely be insufficient to account for the methane seasonality and they are often assumed aseasonal in global and regional inventories (e.g. Crippa et al., 2020; Maasakkers et al., 2023). Emissions due to building energy consumption peak in NH winter but are relatively small at an estimated 12 Tg a⁻¹ (Crippa et al., 2020). Emissions from manure management are also relatively small (Table 1) and depend on temperature in a way that is well understood (Chadwick et al., 2011). GEOS-Chem model transport errors at the 2° × 2.5° resolution used here show no indication of systematic bias (Stanevich et al., 2020). Biases in non-seasonal sources can affect the magnitude of the seasonal bias but not significantly its phase.

3 Conclusions

Surface and satellite observations of atmospheric methane show a sharp mid-summer increase in the Northern Hemisphere (NH) that is not reproduced by the GEOS-Chem chemical transport model driven by its default representations of sources and sinks. Such a bias could affect global inverse analyses of atmospheric observations using these sources and sinks as prior estimates. Using an ensemble of model simulations, we find that the seasonality and latitudinal distribution of NH wetland emissions are the most likely causes of the seasonal methane bias. In contrast, the seasonality of the OH sink is consistent across models. Other seasonal terms in the methane budget are not sufficiently large to have significant effect on the bias. Of the 24 wetland emission inventories considered in our ensemble, we find that the LPJ-wsl with MERRA-2 meteorology is the only one that reproduces the observed NH seasonality of atmospheric methane in different latitude bands. This is because of two attributes: (1) a large emission of 80 Tg a⁻¹ from NH wetlands north of 10°N, including a significant contribution at 10°-35°N from South Asia, and (2) the timing of boreal emissions with a delayed spring start, an August peak, and persistence into autumn, reflecting the use of soil temperature to estimate heterotrophic respiration and the representation of freeze-thaw dynamics and snow cover. These insights can inform studies of past and future atmospheres. Prior wetland emission estimates used for inverse modeling should reflect the two attributes named above. Optimization of OH concentrations as part of these inversions should separate the two hemispheres, with appropriate error correlations (Penn et al., 2023).

Acknowledgments

This work was supported by the NASA Carbon Monitoring System (CMS) and the NOAA AC4 programs. Portions of this research were carried out at the Jet Propulsion Laboratory, California Institute of Technology, under a contract with the National Aeronautics and Space Administration. We acknowledge the modeling groups participating in ACCMIP and CCMI for making their simulations available for this analysis, the joint WCRP SPARC/IGAC Chemistry-Climate Model Initiative (CCMI) for organizing and coordinating the model data analysis activity, and the British Atmospheric Data Centre (BADC) for collecting and archiving the CCMI model output.

Open Research

The ACCMIP OH distributions can be downloaded from <http://catalogue.ceda.ac.uk/uuid/ded523bf23d59910e5d73f1703a2d540> (Shindell et al., 2011). The CCM1-1 OH distributions can be downloaded from <https://catalogue.ceda.ac.uk/uuid/9cc6b94df0f4469d8066d69b5df879d5> (Hegglin et al., 2015). The blended TROPOMI+GOSAT methane satellite data can be downloaded from <https://dataverse.harvard.edu/dataverse/blended-tropomi-gosat-methane> (Balasus, 2023). The NOAA surface observations can be downloaded from <https://gml.noaa.gov/ccgg/data/ch4.html> (Schuldt et al., 2023). The GEOS-Chem code used in this study is archived at <https://zenodo.org/records/7600404> (Yantosca et al., 2023).

References

- Balasus, N. (2023). Blended TROPOMI+GOSAT Satellite Data Product for Atmospheric Methane [Data set]. Harvard Dataverse. Retrieved from <https://dataverse.harvard.edu/dataverse/blended-tropomi-gosat-methane>
- Balasus, N., Jacob, D. J., Lorente, A., Maasakkers, J. D., Parker, R. J., Boesch, H., et al. (2023). A blended TROPOMI+GOSAT satellite data product for atmospheric methane using machine learning to correct retrieval biases. *Atmospheric Measurement Techniques*, 16(16), 3787–3807. <https://doi.org/10.5194/amt-16-3787-2023>
- Bao, T., Xu, X., Jia, G., Billesbach, D. P., & Sullivan, R. C. (2021). Much stronger tundra methane emissions during autumn freeze than spring thaw. *Global Change Biology*, 27(2), 376–387. <https://doi.org/10.1111/gcb.15421>
- Bergamaschi, P., Karstens, U., Manning, A. J., Saunois, M., Tsuruta, A., Berchet, A., et al. (2018). Inverse modelling of European CH₄ emissions during 2006–2012 using different inverse models and reassessed atmospheric observations. *Atmospheric Chemistry and Physics*, 18(2), 901–920. <https://doi.org/10.5194/acp-18-901-2018>
- Bloom, A. A., Exbrayat, J.-F., Van Der Velde, I. R., Feng, L., & Williams, M. (2016). The decadal state of the terrestrial carbon cycle: Global retrievals of terrestrial carbon allocation, pools, and residence times. *Proceedings of the National Academy of Sciences*, 113(5), 1285–1290. <https://doi.org/10.1073/pnas.1515160113>
- Bloom, A. A., Bowman, K. W., Lee, M., Turner, A. J., Schroeder, R., Worden, J. R., et al. (2017). A global wetland methane emissions and uncertainty dataset for atmospheric chemical transport models (WetCHARTs version 1.0). *Geoscientific Model Development*, 10(6), 2141–2156. <https://doi.org/10.5194/gmd-10-2141-2017>
- Chadwick, D., Sommer, S., Thorman, R., Fangueiro, D., Cardenas, L., Amon, B., & Misselbrook, T. (2011). Manure management: Implications for greenhouse gas emissions. *Animal Feed Science and Technology*, 166–167, 514–531. <https://doi.org/10.1016/j.anifeedsci.2011.04.036>
- Chandra, N., Hayashida, S., Saeki, T., & Patra, P. K. (2017). What controls the seasonal cycle of columnar methane observed by GOSAT over different regions in India? *Atmospheric Chemistry and Physics*, 17(20), 12633–12643. <https://doi.org/10.5194/acp-17-12633-2017>
- Chang, K.-Y., Riley, W. J., Knox, S. H., Jackson, R. B., McNicol, G., Poulter, B., et al. (2021). Substantial hysteresis in emergent temperature sensitivity of global wetland CH₄ emissions. *Nature Communications*, 12(1), 2266. <https://doi.org/10.1038/s41467-021-22452-1>

- Chen, Z., Jacob, D. J., Gautam, R., Omara, M., Stavins, R. N., Stowe, R. C., et al. (2023). Satellite quantification of methane emissions and oil–gas methane intensities from individual countries in the Middle East and North Africa: implications for climate action. *Atmospheric Chemistry and Physics*, 23(10), 5945–5967. <https://doi.org/10.5194/acp-23-5945-2023>
- Crippa, M., Solazzo, E., Huang, G., Guizzardi, D., Koffi, E., Muntean, M., et al. (2020). High resolution temporal profiles in the Emissions Database for Global Atmospheric Research. *Scientific Data*, 7(1), 121. <https://doi.org/10.1038/s41597-020-0462-2>
- Curry, C. L. (2007). Modeling the soil consumption of atmospheric methane at the global scale. *Global Biogeochemical Cycles*, 21(4), n/a–n/a. <https://doi.org/10.1029/2006GB002818>
- Delwiche, K. B., Knox, S. H., Malhotra, A., Fluet-Chouinard, E., McNicol, G., Feron, S., et al. (2021). FLUXNET-CH4: a global, multi-ecosystem dataset and analysis of methane seasonality from freshwater wetlands. *Earth System Science Data*, 13(7), 3607–3689. <https://doi.org/10.5194/essd-13-3607-2021>
- Dlugokencky, E. J., Masarie, K. A., Tans, P. P., Conway, T. J., & Xiong, X. (1997). Is the amplitude of the methane seasonal cycle changing? *Atmospheric Environment*, 31(1), 21–26. [https://doi.org/10.1016/S1352-2310\(96\)00174-4](https://doi.org/10.1016/S1352-2310(96)00174-4)
- Dowd, E., Wilson, C., Chipperfield, M. P., Gloor, E., Manning, A., & Doherty, R. (2023). Decreasing seasonal cycle amplitude of methane in the northern high latitudes being driven by lower latitude changes in emissions and transport. *Atmospheric Chemistry and Physics*, 23. <https://doi.org/10.5194/egusphere-2023-132>
- Eastham, S. D., Weisenstein, D. K., & Barrett, S. R. H. (2014). Development and evaluation of the unified tropospheric–stratospheric chemistry extension (UCX) for the global chemistry-transport model GEOS-Chem. *Atmospheric Environment*, 89, 52–63. <https://doi.org/10.1016/j.atmosenv.2014.02.001>
- Feng, L., Palmer, P. I., Parker, R. J., Lunt, M. F., & Bösch, H. (2023). Methane emissions are predominantly responsible for record-breaking atmospheric methane growth rates in 2020 and 2021. *Atmos. Chem. Phys.*
- Hegglin, M. I., Lamarque, J.-F., & Eyring, V. (2015). The IGAC/SPARC Chemistry-Climate Model Initiative Phase-1 (CCMI-1) model data output [Data set]. NCAS British Atmospheric Data Centre. Retrieved from <http://catalogue.ceda.ac.uk/uuid/9cc6b94df0f4469d8066d69b5df879d5>
- Houweling, S., Bergamaschi, P., Chevallier, F., Heimann, M., Kaminski, T., Krol, M., et al. (2017). Global inverse modeling of CH4 sources and sinks: an overview of methods. *Atmospheric Chemistry and Physics*, 17(1), 235–256. <https://doi.org/10.5194/acp-17-235-2017>
- IPCC. (2021). *Climate Change 2021 – The Physical Science Basis: Working Group I Contribution to the Sixth Assessment Report of the Intergovernmental Panel on Climate Change* (1st ed.). Cambridge University Press. <https://doi.org/10.1017/9781009157896>
- Ito, A., Li, T., Qin, Z., Melton, J. R., Tian, H., Kleinen, T., et al. (2023). Cold-Season Methane Fluxes Simulated by GCP-CH4 Models. *Geophysical Research Letters*, 50(14), e2023GL103037. <https://doi.org/10.1029/2023GL103037>
- Jacob, D. J., Turner, A. J., Maasakkers, J. D., Sheng, J., Sun, K., Liu, X., et al. (2016). Satellite observations of atmospheric methane and their value for quantifying methane emissions. *Atmospheric Chemistry and Physics*, 16(22), 14371–14396. <https://doi.org/10.5194/acp-16-14371-2016>

- Kirschke, S., Bousquet, P., Ciais, P., Saunois, M., Canadell, J. G., Dlugokencky, E. J., et al. (2013). Three decades of global methane sources and sinks. *Nature Geoscience*, 6(10), 813–823. <https://doi.org/10.1038/ngeo1955>
- Kivimäki, E., Lindqvist, H., Hakkarainen, J., Laine, M., Sussmann, R., Tsuruta, A., et al. (2019). Evaluation and Analysis of the Seasonal Cycle and Variability of the Trend from GOSAT Methane Retrievals. *Remote Sensing*, 11(7), 882. <https://doi.org/10.3390/rs11070882>
- Lamarque, J. F., Shindell, D. T., Josse, B., Young, P. J., Cionni, I., Eyring, V., et al. (2013). The atmospheric chemistry and climate model intercomparison Project (ACCMIP): Overview and description of models, simulations and climate diagnostics. *Geoscientific Model Development*, 6(1), 179–206. <https://doi.org/10.5194/gmd-6-179-2013>
- Liu, T., Mickley, L. J., Marlier, M. E., DeFries, R. S., Khan, M. F., Latif, M. T., & Karambelas, A. (2020). Diagnosing spatial biases and uncertainties in global fire emissions inventories: Indonesia as regional case study. *Remote Sensing of Environment*, 237, 111557. <https://doi.org/10.1016/j.rse.2019.111557>
- Ma, S., Worden, J. R., Bloom, A. A., Zhang, Y., Poulter, B., Cusworth, D. H., et al. (2021). Satellite Constraints on the Latitudinal Distribution and Temperature Sensitivity of Wetland Methane Emissions. *AGU Advances*, 2(3). <https://doi.org/10.1029/2021AV000408>
- Maasakkers, J. D., Jacob, D. J., Sulprizio, M. P., Turner, A. J., Weitz, M., Wirth, T., et al. (2016). Gridded National Inventory of U.S. Methane Emissions. *Environmental Science & Technology*, 50(23), 13123–13133. <https://doi.org/10.1021/acs.est.6b02878>
- Maasakkers, J. D., Jacob, D. J., Sulprizio, M. P., Scarpelli, T. R., Nesser, H., Sheng, J.-X., et al. (2019). Global distribution of methane emissions, emission trends, and OH concentrations and trends inferred from an inversion of GOSAT satellite data for 2010–2015. *Atmospheric Chemistry and Physics*, 19(11), 7859–7881. <https://doi.org/10.5194/acp-19-7859-2019>
- Maasakkers, J. D., McDuffie, E. E., Sulprizio, M. P., Chen, C., Schultz, M., Brunelle, L., et al. (2023). A Gridded Inventory of Annual 2012–2018 U.S. Anthropogenic Methane Emissions. *Environmental Science & Technology*, 57(43), 16276–16288. <https://doi.org/10.1021/acs.est.3c05138>
- Mooring, T. A., Jacob, D. J., Sulprizio, M. P., Balasus, N., Baier, B. C., Kiefer, M., et al. (2024). Evaluating Stratospheric Methane in GEOS-Chem with Satellite and Balloon Observations. Presented at the American Meteorological Society 104th Annual Meeting, Baltimore, MD, USA. Retrieved from <https://ams.confex.com/ams/104ANNUAL/meetingapp.cgi/Paper/437083>
- Morgenstern, O., Hegglin, M. I., Rozanov, E., O'Connor, F. M., Abraham, N. L., Akiyoshi, H., et al. (2017). Review of the global models used within phase 1 of the Chemistry–Climate Model Initiative (CCMI). *Geoscientific Model Development*, 10(2), 639–671. <https://doi.org/10.5194/gmd-10-639-2017>
- Murguía-Flores, F., Arndt, S., Ganesan, A. L., Murray-Tortarolo, G., & Hornibrook, E. R. C. (2018). Soil Methanotrophy Model (MeMo v1.0): a process-based model to quantify global uptake of atmospheric methane by soil. *Geoscientific Model Development*, 11(6), 2009–2032. <https://doi.org/10.5194/gmd-11-2009-2018>
- Naik, V., Voulgarakis, A., Fiore, A. M., Horowitz, L. W., Lamarque, J.-F., Lin, M., et al. (2013). Preindustrial to present-day changes in tropospheric hydroxyl radical and methane lifetime from the Atmospheric Chemistry and Climate Model Intercomparison Project (ACCMIP). *Atmospheric Chemistry and Physics*, 13(10), 5277–5298. <https://doi.org/10.5194/acp-13-5277-2013>
- Naus, S., Montzka, S. A., Patra, P. K., & Krol, M. C. (2021). A three-dimensional-model inversion of methyl chloroform to constrain the atmospheric oxidative capacity. *Atmos. Chem. Phys.*

- 478 Nazaries, L., Murrell, J. C., Millard, P., Baggs, L., & Singh, B. K. (2013). Methane, microbes and
479 models: fundamental understanding of the soil methane cycle for future predictions.
480 *Environmental Microbiology*, 15(9), 2395–2417. <https://doi.org/10.1111/1462-2920.12149>
- 481 Nelson, K., Thompson, D., Hopkinson, C., Petrone, R., & Chasmer, L. (2021). Peatland-fire interactions:
482 A review of wildland fire feedbacks and interactions in Canadian boreal peatlands. *Science of The*
483 *Total Environment*, 769, 145212. <https://doi.org/10.1016/j.scitotenv.2021.145212>
- 484 NOAA GML. (2023, September 18). NOAA Greenhouse Gas Marine Boundary Layer Reference Site
485 Map for CH₄. Retrieved from <https://gml.noaa.gov/ccgg/mbl/map.php?param=CH4>
- 486 Olefeldt, D., Turetsky, M. R., Crill, P. M., & McGuire, A. D. (2013). Environmental and physical
487 controls on northern terrestrial methane emissions across permafrost zones. *Global Change*
488 *Biology*, 19(2), 589–603. <https://doi.org/10.1111/gcb.12071>
- 489 Orbe, C., Plummer, D. A., Waugh, D. W., Yang, H., Jöckel, P., Kinnison, D. E., et al. (2020). Description
490 and Evaluation of the specified-dynamics experiment in the Chemistry-Climate Model Initiative.
491 *Atmospheric Chemistry and Physics*, 20(6), 3809–3840. [https://doi.org/10.5194/acp-20-3809-](https://doi.org/10.5194/acp-20-3809-2020)
492 2020
- 493 Palmer, P. I., Feng, L., Lunt, M. F., Parker, R. J., Bösch, H., Lan, X., et al. (2021). The added value of
494 satellite observations of methane for understanding the contemporary methane budget.
495 *Philosophical Transactions of the Royal Society A: Mathematical, Physical and Engineering*
496 *Sciences*, 379(2210), 20210106. <https://doi.org/10.1098/rsta.2021.0106>
- 497 Parker, R. J., Wilson, C., Bloom, A. A., Comyn-Platt, E., Hayman, G., McNorton, J., et al. (2020).
498 Exploring constraints on a wetland methane emission ensemble (WetCHARTs) using GOSAT
499 observations. *Biogeosciences*, 17(22), 5669–5691. <https://doi.org/10.5194/bg-17-5669-2020>
- 500 Patra, P. K., Krol, M. C., Montzka, S. A., Arnold, T., Atlas, E. L., Lintner, B. R., et al. (2014).
501 Observational evidence for interhemispheric hydroxyl-radical parity. *Nature*, 513(7517), 219–
502 223. <https://doi.org/10.1038/nature13721>
- 503 Patra, P. K., Krol, M. C., Prinn, R. G., Takigawa, M., Mühle, J., Montzka, S. A., et al. (2021). Methyl
504 Chloroform Continues to Constrain the Hydroxyl (OH) Variability in the Troposphere. *Journal of*
505 *Geophysical Research: Atmospheres*, 126(4), e2020JD033862.
506 <https://doi.org/10.1029/2020JD033862>
- 507 Penn, E., Jacob, D. J., Worden, J. R., Zhang, Y., Nesser, H., Qu, Z., et al. (2023). What can we learn
508 about OH from satellite observations of methane? A41C-08. Presented at the AGU Annual
509 Meeting, San Francisco, CA, USA. Retrieved from
510 <https://agu.confex.com/agu/fm23/meetingapp.cgi/Paper/1284287>
- 511 Peters, C. N., Bennartz, R., & Hornberger, G. M. (2017). Satellite-derived methane emissions from
512 inundation in Bangladesh. *Journal of Geophysical Research: Biogeosciences*, 122(5), 1137–1155.
513 <https://doi.org/10.1002/2016JG003740>
- 514 Pickett-Heaps, C. A., Jacob, D. J., Wecht, K. J., Kort, E. A., Wofsy, S. C., Diskin, G. S., et al. (2011).
515 Magnitude and seasonality of wetland methane emissions from the Hudson Bay Lowlands
516 (Canada). *Atmospheric Chemistry and Physics*, 11(8), 3773–3779. [https://doi.org/10.5194/acp-](https://doi.org/10.5194/acp-11-3773-2011)
517 11-3773-2011
- 518 Portmann, F. T., Siebert, S., & Döll, P. (2010). MIRCA2000—Global monthly irrigated and rainfed crop
519 areas around the year 2000: A new high-resolution data set for agricultural and hydrological
520 modeling. *Global Biogeochemical Cycles*, 24(1), 2008GB003435.
521 <https://doi.org/10.1029/2008GB003435>

- Prather, M. J., Holmes, C. D., & Hsu, J. (2012). Reactive greenhouse gas scenarios: Systematic exploration of uncertainties and the role of atmospheric chemistry. *Geophysical Research Letters*, 39(9), 2012GL051440. <https://doi.org/10.1029/2012GL051440>
- Priemé, A., & Christensen, S. (1997). Seasonal and spatial variation of methane oxidation in a Danish spruce forest. *Soil Biology and Biochemistry*, 29(8), 1165–1172. [https://doi.org/10.1016/S0038-0717\(97\)00038-2](https://doi.org/10.1016/S0038-0717(97)00038-2)
- Rocher-Ros, G., Stanley, E. H., Loken, L. C., Casson, N. J., Raymond, P. A., Liu, S., et al. (2023). Global methane emissions from rivers and streams. *Nature*. <https://doi.org/10.1038/s41586-023-06344-6>
- Saunio, M., Stavert, A. R., Poulter, B., Bousquet, P., Canadell, J. G., Jackson, R. B., et al. (2020). The Global Methane Budget 2000–2017. *Earth System Science Data*, 12(3), 1561–1623. <https://doi.org/10.5194/essd-12-1561-2020>
- Scarpelli, T. R., Jacob, D. J., Octaviano Villasana, C. A., Ramírez Hernández, I. F., Cárdenas Moreno, P. R., Cortés Alfaro, E. A., et al. (2020). A gridded inventory of anthropogenic methane emissions from Mexico based on Mexico's national inventory of greenhouse gases and compounds. *Environmental Research Letters*, 15(10), 105015. <https://doi.org/10.1088/1748-9326/abb42b>
- Scarpelli, T. R., Jacob, D. J., Moran, M., Reuland, F., & Gordon, D. (2022a). A gridded inventory of Canada's anthropogenic methane emissions. *Environmental Research Letters*, 17(1), 014007. <https://doi.org/10.1088/1748-9326/ac40b1>
- Scarpelli, T. R., Jacob, D. J., Grossman, S., Lu, X., Qu, Z., Sulprizio, M. P., et al. (2022b). Updated Global Fuel Exploitation Inventory (GFEI) for methane emissions from the oil, gas, and coal sectors: evaluation with inversions of atmospheric methane observations. *Atmospheric Chemistry and Physics*, 22(5), 3235–3249. <https://doi.org/10.5194/acp-22-3235-2022>
- Schuldt, K. N., Aalto, T., Andrews, A., Aoki, S., Apadula, F., Arduini, J., et al. (2023). Multi-laboratory compilation of atmospheric methane data for the period 1983–2021. obspack_ch4_1_GLOBALVIEWplus_v5.1_2023-03-08 [Data set]. NOAA Earth System Research Laboratory, Global Monitoring Laboratory. <https://doi.org/10.25925/20230301>
- Shindell, D., Lamarque, J. F., Collins, W., Eyring, V., Nagashima, T., Naik, V., et al. (2011). The model data outputs from the Atmospheric Chemistry & Climate Model Intercomparison Project (ACCMIP) [Data set]. NERC EDS Centre for Environmental Data Analysis. Retrieved from <http://catalogue.ceda.ac.uk/uuid/ded523bf23d59910e5d73f1703a2d540>
- Stanevich, I., Jones, D. B. A., Strong, K., Parker, R. J., Boesch, H., Wunch, D., et al. (2020). Characterizing model errors in chemical transport modeling of methane: impact of model resolution in versions v9-02 of GEOS-Chem and v35j of its adjoint model. *Geoscientific Model Development*, 13(9), 3839–3862. <https://doi.org/10.5194/gmd-13-3839-2020>
- Treat, C. C., Bloom, A. A., & Marushchak, M. E. (2018). Nongrowing season methane emissions—a significant component of annual emissions across northern ecosystems. *Global Change Biology*, 24(8), 3331–3343. <https://doi.org/10.1111/gcb.14137>
- Tsuruta, A., Kivimäki, E., Lindqvist, H., Karppinen, T., Backman, L., Hakkarainen, J., et al. (2023). CH4 Fluxes Derived from Assimilation of TROPOMI XCH4 in CarbonTracker Europe-CH4: Evaluation of Seasonality and Spatial Distribution in the Northern High Latitudes. *Remote Sensing*, 15(6), 1620. <https://doi.org/10.3390/rs15061620>
- Turetsky, M. R., Amiro, B. D., Bosch, E., & Bhatti, J. S. (2004). Historical burn area in western Canadian peatlands and its relationship to fire weather indices. *Global Biogeochemical Cycles*, 18(4), n/a–n/a. <https://doi.org/10.1029/2004GB002222>

- Turner, A. J., Frankenberg, C., Wennberg, P. O., & Jacob, D. J. (2017). Ambiguity in the causes for decadal trends in atmospheric methane and hydroxyl. *Proceedings of the National Academy of Sciences*, 114(21), 5367–5372. <https://doi.org/10.1073/pnas.1616020114>
- Van Der Werf, G. R., Randerson, J. T., Giglio, L., Van Leeuwen, T. T., Chen, Y., Rogers, B. M., et al. (2017). Global fire emissions estimates during 1997–2016. *Earth System Science Data*, 9(2), 697–720. <https://doi.org/10.5194/essd-9-697-2017>
- Wang, X., Jacob, D. J., Eastham, S. D., Sulprizio, M. P., Zhu, L., Chen, Q., et al. (2019). The role of chlorine in global tropospheric chemistry. *Atmospheric Chemistry and Physics*, 19(6), 3981–4003. <https://doi.org/10.5194/acp-19-3981-2019>
- Wania, R., Ross, I., & Prentice, I. C. (2009). Integrating peatlands and permafrost into a dynamic global vegetation model: 1. Evaluation and sensitivity of physical land surface processes: PEATLANDS AND PERMAFROST IN LPJ, 1. *Global Biogeochemical Cycles*, 23(3). <https://doi.org/10.1029/2008GB003412>
- Warwick, N. J., Cain, M. L., Fisher, R., France, J. L., Lowry, D., Michel, S. E., et al. (2016). Using d13C-CH₄ and dD-CH₄ to constrain Arctic methane emissions. *Atmospheric Chemistry and Physics*, 16(23), 14891–14908. <https://doi.org/10.5194/acp-16-14891-2016>
- Wecht, K. J., Jacob, D. J., Frankenberg, C., Jiang, Z., & Blake, D. R. (2014). Mapping of North American methane emissions with high spatial resolution by inversion of SCIAMACHY satellite data. *Journal of Geophysical Research: Atmospheres*, 119(12), 7741–7756. <https://doi.org/10.1002/2014JD021551>
- Worden, J. R., Cusworth, D. H., Qu, Z., Yin, Y., Zhang, Y., Bloom, A. A., et al. (2022). The 2019 methane budget and uncertainties at 1° resolution and each country through Bayesian integration Of GOSAT total column methane data and a priori inventory estimates. *Atmospheric Chemistry and Physics*, 22(10), 6811–6841. <https://doi.org/10.5194/acp-22-6811-2022>
- Yantosca, B., Sulprizio, M., Lundgren, L., Kelvinhb, Keller, C., Fritz, T., et al. (2023, February 2). geoschem/geos-chem: GEOS-Chem 14.1.0 [Software] (Version 14.1.0). Zenodo. <https://doi.org/10.5281/ZENODO.7600404>
- Yu, X., Millet, D. B., & Henze, D. K. (2021). How well can inverse analyses of high-resolution satellite data resolve heterogeneous methane fluxes? Observing system simulation experiments with the GEOS-Chem adjoint model (v35). *Geoscientific Model Development*, 14(12), 7775–7793. <https://doi.org/10.5194/gmd-14-7775-2021>
- Yu, X., Millet, D. B., Henze, D. K., Turner, A. J., Delgado, A. L., Bloom, A. A., & Sheng, J. (2023). A high-resolution satellite-based map of global methane emissions reveals missing wetland, fossil fuel, and monsoon sources. *Atmospheric Chemistry and Physics*, 23(5), 3325–3346. <https://doi.org/10.5194/acp-23-3325-2023>
- Zhang, B., Tian, H., Ren, W., Tao, B., Lu, C., Yang, J., et al. (2016a). Methane emissions from global rice fields: Magnitude, spatiotemporal patterns, and environmental controls. *Global Biogeochemical Cycles*, 30(9), 1246–1263. <https://doi.org/10.1002/2016GB005381>
- Zhang, G., Xiao, X., Dong, J., Xin, F., Zhang, Y., Qin, Y., et al. (2020). Fingerprint of rice paddies in spatial–temporal dynamics of atmospheric methane concentration in monsoon Asia. *Nature Communications*, 11(1), 554. <https://doi.org/10.1038/s41467-019-14155-5>
- Zhang, Y., Jacob, D. J., Lu, X., Maasakkers, J. D., Scarpelli, T. R., Sheng, J.-X., et al. (2021). Attribution of the accelerating increase in atmospheric methane during 2010–2018 by inverse analysis of GOSAT observations. *Atmospheric Chemistry and Physics*, 21(5), 3643–3666. <https://doi.org/10.5194/acp-21-3643-2021>

- 611 Zhang, Y., Fang, S., Chen, J., Lin, Y., Chen, Y., Liang, R., et al. (2022). Observed changes in China's
612 methane emissions linked to policy drivers. *Proceedings of the National Academy of Sciences*,
613 *119*(41), e2202742119. <https://doi.org/10.1073/pnas.2202742119>
- 614 Zhang, Z., Zimmermann, N. E., Kaplan, J. O., & Poulter, B. (2016b). Modeling spatiotemporal dynamics
615 of global wetlands: comprehensive evaluation of a new sub-grid TOPMODEL parameterization
616 and uncertainties. *Biogeosciences*, *13*(5), 1387–1408. <https://doi.org/10.5194/bg-13-1387-2016>
- 617 Zhang, Z., Zimmermann, N. E., Calle, L., Hurtt, G., Chatterjee, A., & Poulter, B. (2018). Enhanced
618 response of global wetland methane emissions to the 2015–2016 El Niño–Southern Oscillation
619 event. *Environmental Research Letters*, *13*(7), 074009. <https://doi.org/10.1088/1748-9326/aac939>

Interpreting the seasonality of atmospheric methane

James D. East¹, Daniel. J. Jacob¹, Nicholas Balasus¹, A. Anthony Bloom², Lori Bruhwiler³, Zichong Chen¹, Jed O. Kaplan⁴, Loretta J. Mickley¹, Todd A. Mooring⁵, Elise Penn⁵, Benjamin Poulter⁶, Melissa P. Sulprizio¹, Robert M. Yantosca¹, John R. Worden², Zhen Zhang⁷

¹ Harvard John A. Paulson School of Engineering and Applied Sciences, Harvard University, Cambridge, MA, USA, 02138

² Jet Propulsion Laboratory, California Institute of Technology, Pasadena, CA, USA 91011

³ NOAA Earth System Research Laboratory, Global Monitoring Division, Boulder, CO, USA 80305

⁴ Department of Earth, Energy, and Environment, University of Calgary, Calgary, Canada

⁵ Department of Earth and Planetary Sciences, Harvard University, Cambridge, MA, USA 02138

⁶ NASA GSFC, Biospheric Sciences Lab, Greenbelt, MD 20771

⁷ State Key Laboratory of Tibetan Plateau Earth System, Environment and Resources (TPESER), Institute of Tibetan Plateau Research, Chinese Academy of Sciences, Beijing, China

Corresponding author: J. D. East, jeast@g.harvard.edu

Contents of this file

Tables S1 to S2

Figures S1 to S3

Introduction

Tables S1 and S2 and Figures S1 to S3 are included below to supplement the main manuscript. Descriptions of each figure and table are included in the caption.

Table S1:OH simulation ensemble members.

Project	Model	Experiment	[OH] _{GM} Air mass weighted 10 ⁵ molecules cm ⁻³	NH/SH
-	GEOS-Chem default		10.0	1.07
-	GEOS-Chem (NH/SH best estimate)		10.0	0.97
-	GEOS-Chem (NH/SH low estimate)		10.0	0.85
-	GEOS-Chem (+10%)		11.0	1.07
-	GEOS-Chem (-10%)		9.0	1.07
ACCMIP	CESM-CAM-superfast	acchist	8.6	1.40
ACCMIP	CICERO-OsloCTM2	acchist	8.3	1.35
ACCMIP	CMAM	acchist	8.9	1.17
ACCMIP	EMAC	acchist	9.5	1.09
ACCMIP	GEOSCCM	acchist	9.9	1.14
ACCMIP	GFDL-AM3	acchist	9.4	1.17
ACCMIP	GISS-E2-R	acchist	8.6	1.20
ACCMIP	MIROC-CHEM	acchist	9.1	1.26
ACCMIP	MOCAGE	acchist	8.6	1.21
ACCMIP	NCAR-CAM3.5	acchist	8.9	1.32
ACCMIP	STOC-HadAM3	acchist	8.2	1.30
ACCMIP	UM-CAM	acchist	9.3	1.34
CCMI	CHASER-MIROC-ESM	REF-C1SD	9.1	1.19
CCMI	CMAM	REF-C1SD	9.1	1.16
CCMI	EMAC-L47MA	REF-C1SD	9.9	1.18
CCMI	EMAC-L90MA	REF-C1SD	9.6	1.20
CCMI	MOCAGE	REF-C1SD	8.2	1.23

Experiments for ACCMIP are described in Lamarque et al. (2013) and experiments for CCMI are described in Orbe et al. (2020). All models are weighted by the same GEOS-Chem atmosphere.

Table S2: Annual wetland emissions in latitude bands and month of boreal peak.

Wetland inventory	Global total [Tg]	-90 to -10 [Tg]	-10 to 10 [Tg]	10 to 35 [Tg]	35 to 90 [Tg]	Boreal peak month
WetCHARTs HP-mean	140	14	82	11	33	July
LPJ-wsl CRU	204	30	115	33	26	August
LPJ-wsl ERA5	158	22	73	21	43	August
LPJ-wsl ERA5-MSWEP	156	20	73	21	41	August
LPJ-wsl MERRA-2	192	27	84	31	48	August
UpCH4	150	47	31	41	31	July
WetCHARTs 1913 (HP)	128	10	58	10	49	July
WetCHARTs 1914 (HP)	125	12	67	8	38	July
WetCHARTs 1923 (HP)	126	13	76	13	25	July
WetCHARTs 1924 (HP)	124	13	84	10	18	July
WetCHARTs 1933 (HP)	126	14	81	14	17	July
WetCHARTs 1934 (HP)	125	14	88	10	12	July
WetCHARTs 2913 (HP)	170	13	78	14	66	July
WetCHARTs 2914 (HP)	167	16	90	10	50	July
WetCHARTs 2923	169	17	101	18	33	July
WetCHARTs 2924 (HP)	166	18	112	13	24	July
WetCHARTs 2933	169	18	108	19	23	July
WetCHARTs 2934	166	18	118	14	16	July
WetCHARTs 3913	213	16	97	17	82	July
WetCHARTs 3914	208	20	112	13	63	July
WetCHARTs 3923	211	21	126	22	42	July
WetCHARTs 3924	207	22	140	16	30	July
WetCHARTs 3933	211	23	135	24	29	July
WetCHARTs 3934	208	23	147	17	20	July

WetCHARTs inventories including “HP” are part of the high-performing ensemble identified by Ma et al. (2021) and are used to create the high-performing mean inventory. Latitude totals may not sum exactly to global total due to rounding.

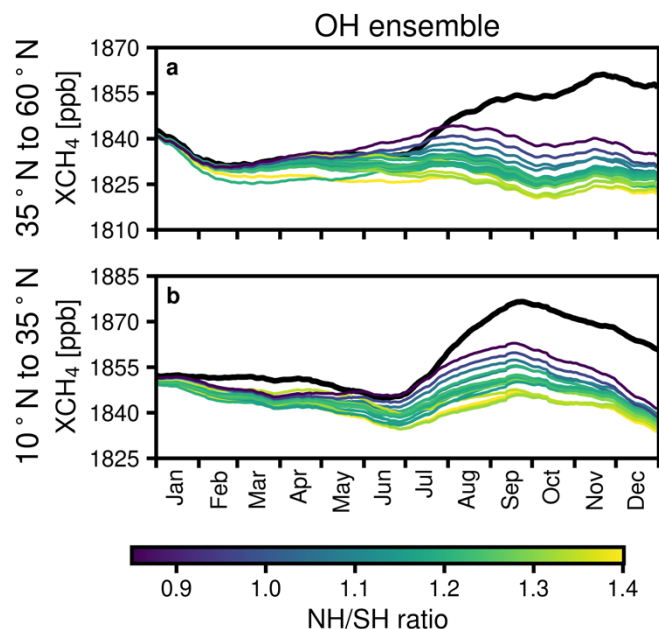


Figure S1: Modeled and observed of dry air column mole fraction of methane (XCH_4), zonally averaged in the latitude bands 10°N-35°N and 35°N-60°N. Black, bold curves represent observations from TROPOMI+GOSAT. Panels (a) and (b) show results for the OH ensemble with each curve representing results from a different GEOS-Chem simulation using OH from a different model colored by NH/SH ratio.

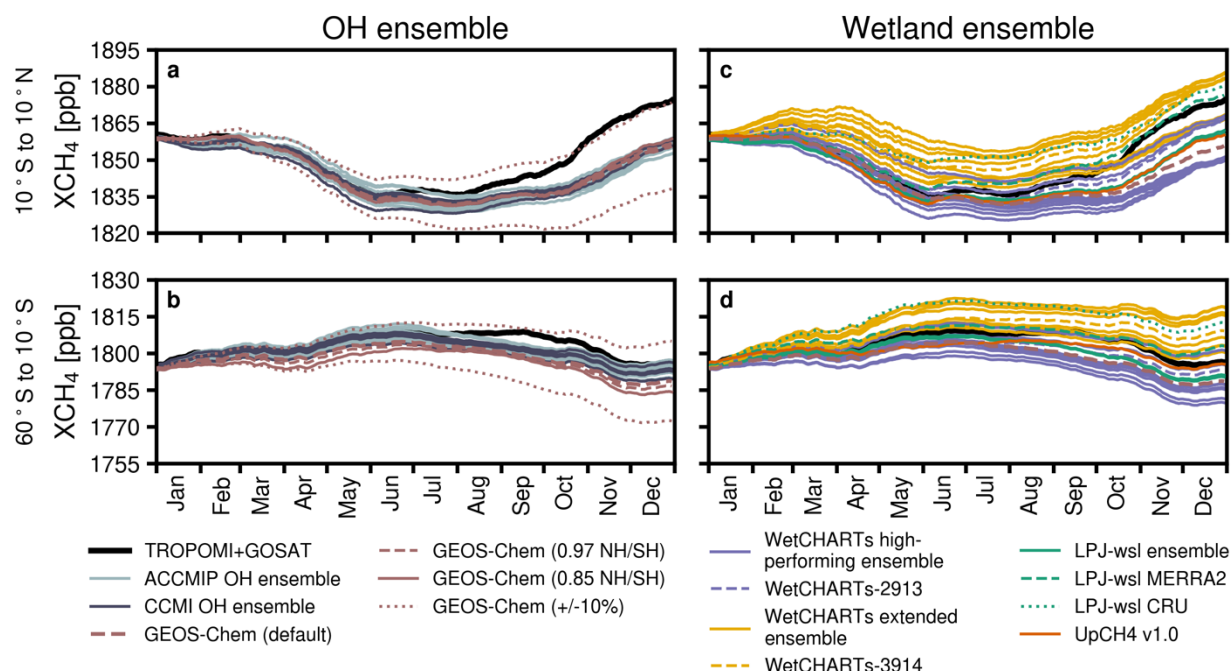


Figure S2: Seasonality of methane for ensembles of OH and wetland simulations, compared to TROPOMI+GOSAT observations at 60°S-10°S and 10°S-10°N. Panels (a) and (b) show results for the OH ensemble with each curve representing results from a different model, and panels (c) and (d) show results for the wetland emissions ensemble. All OH models have been normalized to yield a methane lifetime of 11.2 years against oxidation by tropospheric OH. Red lines in panels (a) and (b) show GEOS-Chem with its default OH, which has a NH/SH ratio of 1.07, and additional simulations with the NH/SH ratio adjusted to 0.97 and 0.85. Dashed and dotted lines in panels (c) and (d) show XCH₄ simulated with selected wetland ensemble members including WetCHARTs-2913, LPJ-wsl MERRA-2, and LPJ-wsl CRU.

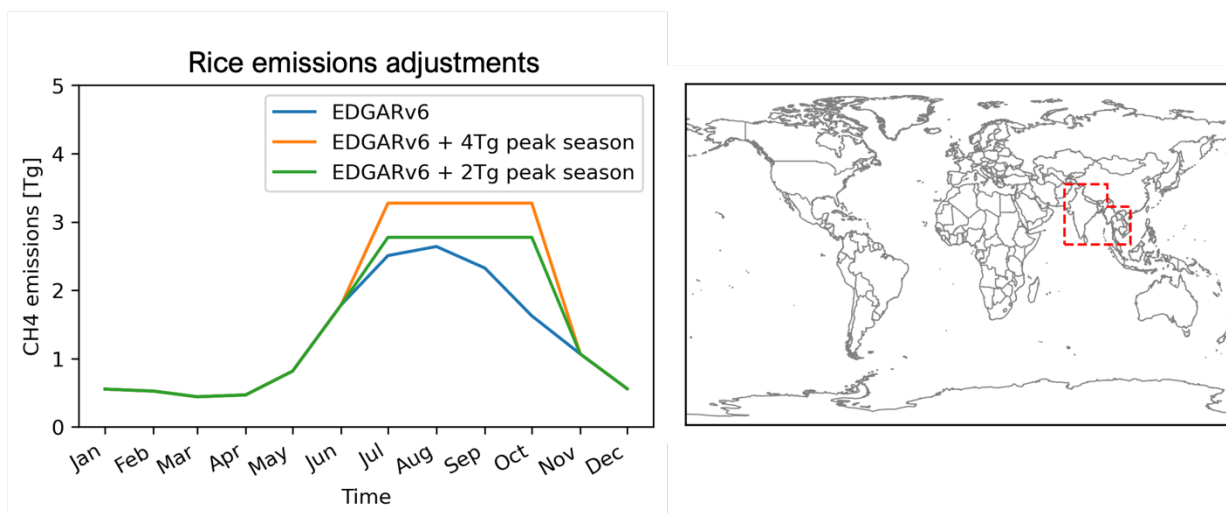


Figure S3: Rice emissions adjustment applied to GEOS-Chem prior emissions, which are EDGARv6. Adjustments are applied only within the red box on the right panel, encompassing India and Southeast Asia. Adjustments increase annual global rice emissions by 4 Tg for the orange line and 2 Tg for the green line.

References

- Lamarque, J. F., Shindell, D. T., Josse, B., Young, P. J., Cionni, I., Eyring, V., et al. (2013). The atmospheric chemistry and climate model intercomparison Project (ACCMIP): Overview and description of models, simulations and climate diagnostics. *Geoscientific Model Development*, 6(1), 179–206. <https://doi.org/10.5194/gmd-6-179-2013>
- Ma, S., Worden, J. R., Bloom, A. A., Zhang, Y., Poulter, B., Cusworth, D. H., et al. (2021). Satellite Constraints on the Latitudinal Distribution and Temperature Sensitivity of Wetland Methane Emissions. *AGU Advances*, 2(3). <https://doi.org/10.1029/2021AV000408>
- Orbe, C., Plummer, D. A., Waugh, D. W., Yang, H., Jöckel, P., Kinnison, D. E., et al. (2020). Description and Evaluation of the specified-dynamics experiment in the Chemistry-Climate Model Initiative. *Atmospheric Chemistry and Physics*, 20(6), 3809–3840. <https://doi.org/10.5194/acp-20-3809-2020>